Faraday Discussions

Molecular Beam Scattering of Ammonia from a Dodecane Flat Liquid Jet

SCHOLARONE™
Manuscripts

Molecular Beam Scattering of Ammonia from a Dodecane Flat Liquid Jet

Steven Saric[1,2†], Walt Yang[1,2†], Daniel M. Neumark[1,2,a)]

[1] *Department of Chemistry, University of California, Berkeley, CA 94720, USA*

[2] *Chemical Sciences Division, Lawrence Berkeley National Laboratory, Berkeley, CA 94720, USA*

[a) Author to whom correspondence should be addressed: dneumark@berkeley.edu

Abstract

The evaporation and scattering of ND_3 from a dodecane flat liquid jet are investigated and the results are compared with previous studies on molecular beam scattering from liquid surfaces. Evaporation is well-described by a Maxwell–Boltzmann flux distribution with a $\cos\theta$ angular distribution at the liquid temperature. Scattering experiments at $E_i = 28.8$ kJ mol^{-1} over a range of deflection angles show evidence for impulsive scattering and thermal desorption. At a deflection angle of 90°, the thermal desorption fraction is 0.49, which is higher than other molecules previously scattered from dodecane and consistent with work performed on NH_3 scattering from a squalane wetted wheel. ND_3 scattering from dodecane results in super-specular scattering, as seen in previous experiments on dodecane. The impulsive scattering channel is fitted to a "soft-sphere" model, yielding an effective surface mass of 55 amu and an internal excitation of 5.08 kJ mol^{-1}. Overall, impulsively scattered ND_3 behaves similarly to other small molecules scattered from dodecane.

Introduction

The gas–liquid interface plays a key role in several processes including acid rain formation, aerosol surface chemistry, and carbon capture at the ocean surface.[1-4] These considerations have motivated the development of experimental techniques to probe structure and reactivity at this interface, including second harmonic and sum-frequency generation spectroscopies,[5] X-ray photoelectron spectroscopy of liquid jets,[6] and mass spectrometry of aerosols created in electrospray ionization.[7] Some of the most insightful work in this area has been carried out by Nathanson and co-workers, whose studies of molecular beam scattering from liquid surfaces have uncovered unprecedented mechanistic detail behind gas–liquid interactions.[8-10]

Molecular beam scattering is a powerful technique that has been used for over a half-century to study chemical dynamics.[11-19] Advances in the field have enabled the elucidation of the dynamics and mechanistic details of gas-phase and gas–surface chemical reactions. The major challenge of extending molecular beam scattering to the gas–liquid interface is that the liquid must be compatible with a high vacuum environment. This ensures that the mean free path is sufficiently large to minimize collisions with the vapor jacket that surrounds a liquid sample. The original molecular beam experiments performed to probe the gas–liquid interface were done with a wetted wheel which allowed for the study of liquids with vapor pressures below 10^{-3} Torr.[20-24]

Experiments on more volatile liquids have been enabled through the efforts of Faubel and co-workers who developed a cylindrical liquid microjet that allows for these liquids to be vacuum compatible.[25, 26] While liquid microjets allow for the study of a larger array of liquid samples than the wetted wheel, they pose specific problems when attempting molecular beam scattering experiments. First, cylindrical jets, which are typically 20 to 30 μm in diameter, present a small

cross-sectional area to an incident molecular beam and thus yield poor signal-to-noise ratios in a scattering experiment. Second, cylindrical microjets do not allow for angularly-resolved scattering measurements.[10] Taking these considerations into account, our group incorporated a flat liquid jet into molecular beam scattering experiments using a microfluidic chip.[27] The flat liquid jet is formed by colliding two cylindrical microjets within the chip to form a flat surface, which provides a much larger scattering target (~1 mm). This simultaneously solves the issues of low signal-to-noise ratios and loss of angular specificity.

The development of the flat liquid jet motivated two recent studies by our research group, in which Ne, CD_4, and D_2O were scattered from dodecane.[28, 29] Dodecane was chosen as a target liquid specifically because of its relatively high vapor pressure (1.5×10^{-2} Torr at 275 K).[26] All scatterers share a mass of 20 amu but differ in their dipole moment, polarizability, and solubility.

Our studies compared two limiting scattering mechanisms: impulsive scattering (IS) and thermal desorption (TD).[28, 29] Impulsive scattering is characterized by an elastic or nearly elastic collision with the surface resulting in a scattered molecule that maintains much of the character of the incident molecular beam. Conversely, thermal desorption is characterized by a scattered particle being trapped at the liquid surface for a period of time long enough to thermalize with the liquid and then evaporate according to a Maxwell–Boltzmann flux distribution at the liquid temperature (T_{liq}).[9, 15, 30, 31]

In our previous work, we demonstrated that both the fractional energy loss and TD fraction, defined as TD/(TD + IS), are higher for the polyatomic molecules than they are for Ne, and trend in a consistent manner with the free energy of solvation found in literature.[29] These results also agreed with previous work performed by Nathanson, in which these same small molecules were

scattered from squalane using a wetted wheel, although his study was confined to a single deflection angle.[32]

In this work, we further probe the evaporation and scattering of small molecules from a dodecane flat liquid jet by investigating deuterated ammonia (ND_3). ND_3 scattering naturally follows from our previous work[28, 29] as it has a mass of 20 amu and has previously been scattered from squalane by Nathanson.[32] This enables further comparison of trends between squalane and dodecane surfaces. ND_3 has very similar physical properties to D_2O as shown in Table 1, apart from its polarizability which is about half that of D_2O.[32-34] Another interesting property of ND_3 is that it has the lowest energy vibrational mode of all of the molecules we have studied thus far: an umbrella inversion mode at 8.95 kJ mol^{-1} (748 cm^{-1}) that could possibly be excited in a collision with the liquid surface. [32, 35-38]

Table 1. Selected physical properties of ND_3 and D_2O.[29, 32-34, 39]

Physical Properties	$ND_3{}^a$	D_2O
Radius (Å)	~1.8	~1.4
Polarizability (Å^3)	1.3	2.2
Dipole Moment (D)	1.4	1.8
Solubility in Hexadecane K_H (x_{soln}/P_{vap})^b	2.97×10^{-2}	2.17×10^{-2}

^{a}Values reported for NH_3.

^{b}Values reported at a partial pressure $P = 1$ atm and a temperature $T = 298.15$ K.

Experimental Methods

The crossed molecular beam apparatus used for all experiments carried out in this work has been previously described in detail.[28, 29, 40, 41] The instrument comprises three regions evacuated by turbomolecular pumps. The source region houses a piezoelectric pulsed valve (MassSpecpecD BV, Enschede) that generates the molecular beam.[42, 43] The collision chamber contains the flat liquid jet and is where gas–liquid interactions take place during scattering experiments. Also present within the collision chamber is a cryogenically cooled copper wall that assists in evacuating this region through cryo-condensation.[28, 29] Finally, the rotatable detector region lies within the collision chamber and houses an electron impact ionizer, a quadrupole mass filter, and an ion detection assembly.[28, 29, 40, 41] A schematic diagram of the scattering experimental configuration is shown in Fig. 1.

The ND_3 supersonic beam is prepared by seeding 1.5 % ND_3 (Sigma–Aldrich 99 % D) in helium. Stagnation conditions through the 500 μm diameter orifice of the valve are 288 K and 3000 Torr with an opening time of 12 μs. This results in a temporal width of 27 μs measured at the detector. The velocity of the molecular beam is characterized by time-of-flight (TOF) measurements with a rotating chopper wheel as described previously.[28, 29] The velocity of the ND_3 molecular beam was measured to be 1718 ± 192 m s^{-1} (FWHM) corresponding to a mean translational kinetic energy of 28.8 kJ mol^{-1}.

The dodecane flat liquid jet is produced by flowing liquid dodecane (n-$C_{12}H_{26}$, TCI America #D0968) through a commercially available microfluidic chip (Micronit BV, Enschede)[27] as described in our previous work.[28, 29] Operating conditions include a flow rate of 3.5 mL min^{-1} and corresponding flow velocity of 10 m s^{-1}, resulting in average dimensions of the flat jet of

1.0×4.5 mm^2 (W $\times$ H). The thickness of the jet is not directly measured but is estimated to be ~ 1.5 μm at its center.[28, 29] Prior to arriving at the microfluidic chip, the liquid is precooled with an in-line counter-current heat exchanger set to 266 K. The average temperature of the liquid in both evaporation and scattering experiments was measured to be 269 K through TOF characterization of molecules evaporating from the jet.

The 3×3 mm^2 detector aperture used throughout leads to a viewing time of ~ 0.5 ms for species detected during all experiments. TOF measurements are taken with the ionizer set to an electron kinetic energy of 80 eV. Each measurement is taken with an acquisition time between 2 and 8 minutes. Time zero for the evaporation experiments is determined by the rotating chopper wheel.[28, 29] In scattering experiments, the short open-time of our pulsed valve enables TOF measurements without the chopper wheel; here, time zero is defined when the most intense part of the pulsed molecular beam collides with the flat liquid jet.

Evaporation experiments are performed by dissolving ND$_3$ in the dodecane reservoir. The dodecane reservoir is initially vacuum degassed for several minutes and then slowly over-pressurized to 850 Torr with the 1.5 % ND$_3$/He mixture. This process is repeated five times. In evaporation experiments, the molecular beam is not present. Scattering experiments are performed by vacuum degassing the dodecane reservoir as described for evaporation, but over-pressurized with pure helium instead of ND$_3$/He.

As shown in the inset of Fig. 1, the incident angle θ_i is defined as the angle between the molecular beam axis and the liquid surface normal, which is set by rotation of the flat liquid jet assembly. In this work, incident angles of 45, 60, and 80° are chosen. The scattering angle θ_f is defined as the angle between the liquid surface normal the detector axis. The deflection angle χ is

defined as $\chi = 180° - (\theta_i + \theta_f)$. In order to prevent systematic errors, TOF measurements are taken in a back-and-forth manner as described previously.[29]

Results and Discussion

Evaporation

Evaporation experiments are used to isolate the TD channel of the scattering experiments and ensure conditions are appropriate for nascent scattering, in which the scattered signal represents gas–liquid rather than gas–vapor collisions. TOF spectra of ND_3 evaporating from the doped dodecane flat jet are shown in Fig. 2 at detector angles θ_f of 0, 30, 60, and 90°. Evaporation samples gas molecules that are thermalized within the liquid, resulting in a particle flux described by a Maxwell–Boltzmann (MB) flux distribution.

$$f_{MB}(v) \propto v^3 \exp\left(-\frac{mv^2}{2RT_{liq}}\right) \#(1)$$

Here, v and m represent the velocity and mass of the evaporating particles, while R is the universal gas constant. TOF profiles for the evaporation of ND_3 from a dodecane flat jet at detector angles $\theta_f = 0$, 30, 60, and 90° are fitted using a linear combination of MB distributions and shown in Fig. 2. The fitting procedure used in Fig. 2 has been described in our prior work.[28, 29] The blue and light blue traces in Fig. 2 show contributions to the TOF spectra that are described by an MB distribution at the liquid temperature T_{liq} and background temperature T_{bkg}, respectively, and the green traces show the sum of these two distributions. The background contribution arises due to desorption of ND_3 from the Cu cryo-cooled wall in the collision chamber that has been experimentally measured to have a temperature of $\sim$118 K in this study.

The TOF spectra for $\theta_f = 0°$ is well-fitted by the T_{liq} MB distribution alone, while spectra at detector angles further away from the surface normal tend to display more "sub-Maxwellian" behavior and have a larger contribution from the T_{bkg} distribution. This trend is explained by the relative flux of evaporated particles from the jet following a $\cos\theta_f$ distribution well-described in the literature.[44, 45]

Integrating the TOF spectra and plotting the intensity as a function of detector angle θ_f results in the angular plot shown in Fig. 3. The angular plot in Fig. 3 shows the T_{liq} MB distributions in blue circles, the T_{bkg} MB distributions in cyan triangles, and the $\cos\theta_f$ distribution with a dashed curve. The T_{liq} distribution is captured by the expected $\cos\theta_f$ distribution from the cosine law of evaporation. Maxwellian behavior of the TOF spectra as well as the T_{liq} distributions fitting the expected $\cos\theta_f$ distribution suggest that ND_3 evaporation from the jet takes place without significant interference from vapor-phase collisions, indicating that scattering experiments should result in nascent scattering from the surface of the flat liquid jet.[28, 29]

Scattering

TOF spectra of ND_3 scattering from a dodecane flat jet at incident angles θ_i of 45, 60, and 80° and various detector angles are shown in Fig. 4. While evaporation can be fully described by TD, scattering is more complicated; however, this process can be simplified significantly by confining the description of scattering to two mechanisms, TD and IS. Unlike TD, which is described by a MB distribution, IS is better described by a supersonic (SS) distribution due to the scattered particles retaining more character of the incident supersonic molecular beam:[9, 31, 46, 47]

$$f_{SS}(v) \propto v^3 \exp\left(-\frac{m(v-v_{SS})^2}{2RT_{SS}}\right) \# (2)$$

Here, v represents the velocity of the particle, R is the universal gas constant, and v_{SS} and T_{SS} are the average flow velocity and average temperature of the molecular beam, respectively. These latter two parameters define an offset and width in velocity space compared to a canonical MB distribution.

As in our previous work, the TOF spectra in Fig. 4 are fitted with the MB distribution corresponding to the liquid temperature shown in blue, the SS distribution shown in red, and the sum of the two distributions shown in green. The blue trace corresponding to the MB distribution is representative of the fraction of the overall scattering events that result in TD, while the red trace corresponding to the SS distribution is representative of the overall scattering events that result in IS. Note that the viewing angle of the detector is estimated to be $\theta_f \pm 0.6°$, resulting in measurable scattering even at $\theta_f = 90°$ where no scattering is expected. A clear trend that persists in the data from Fig. 4 is that larger values of θ_f result in smaller TD fractions. This trend, also seen in our previous work, arises because at these angles the cosine law dictates that the TD flux will be small.[48, 49] The trend for θ_i is similar, in that as θ_i increases, the scattering angle becomes more grazing in nature, also leading to smaller TD fractions. This can be seen by comparing the three spectra at the largest scattering angles.

The TOF spectra from Fig. 4 were integrated to produce the angular plots shown in Fig. 5. The MB distributions corresponding to the TD mechanism are plotted on Fig. 5 as blue squares, the SS distributions corresponding to the IS mechanism are plotted as red circles, and the cosine distribution is once again plotted as a dashed curve whose amplitude matches the values of the blue squares. Each angular plot shows the specular angle as a large black arrow for reference.

Overall, the MB distributions tend to follow a $\cos\theta_f$ trend as expected from TD. The SS distributions tend to peak in intensity near the specular angle for all three incident angles measured as expected of IS. However, the actual peak intensities for the $\theta_i = 45$ and 60° angular plots occur at angles slightly larger than the specular angle. This "super-specular" scattering is well-known to occur in gas–solid scattering.[50, 51] This effect was also observed in our previous work on Ne, CD_4, and D_2O and has been attributed to anisotropic momentum loss being favored parallel to the surface normal.[29]

Kinematic Models

The scattering IS channel is fitted to a "soft-sphere" kinematic model. This model is well-described in the literature and allows for estimating the fractional energy loss of impulsively scattered molecules according to the equation below.[8, 52-54]

$$\left(\frac{\Delta E}{E_i}\right) \approx \frac{2\mu}{(1+\mu)^2}\left[1 + \mu(\sin\chi)^2 - \cos\chi\sqrt{1 - \mu^2(\sin\chi)^2 - \frac{E_{int}}{E_i}(\mu+1) + \frac{E_{int}}{E_i}\left(\frac{\mu+1}{2\mu}\right)}\right]\left[1 + \frac{V - 2RT_{liq}}{E_i}\right] \quad (3)\#$$

Here, ΔE represents the change in translational energy of the scattered molecule and E_i is the incident translational energy of the scattered molecule. The mass ratio between the scattered molecule and the effective surface mass is represented by $\mu = m_{gas}/m_{eff}$. The deflection angle is represented by χ as described earlier. E_{int} is the total internal energy of both the scattered gas molecule and the liquid surface, T_{liq} is the temperature of the liquid surface, and V represents the gas–surface potential, calculated to be 2.8 kJ mol^{-1} using combining rules on the Lennard-Jones parameters listed by Mourits and Rummens for NH_3 and dodecane.[55, 56]

Fractional energy loss as a function of deflection angle is plotted for ND_3 scattering in Fig. 6. ND_3 scattering on dodecane is relatively well-fitted by the soft-sphere model across the entire

data set. Fractional energy loss increases with deflection angle for all incident angles.[28, 29, 53] Similarly, the fractional energy loss is independent of incident angle for a given deflection angle. The effective surface mass is 55 amu which corresponds to only part of a dodecane molecule contributing to each ND_3 collision. The total internal energy of the impulsively scattered ND_3 and surface was determined to be 5.08 kJ mol^{-1} using the soft-sphere fitting model.

By assuming that internal energy loss only occurs along the normal component of the incident velocity of the scattered species, E_{int} is used to calculate an estimation of the super-specular scattering angles. This analysis results in a deviation away from specular scattering corresponding to an increase of ~10° for each θ_i of ND_3 scattered on a dodecane surface. This value matches well with the $\theta_i = 60°$ plot from Fig. 5, where the angle of maximum intensity appears to be approximately 70°, but it does not agree well with the data for incident angles of 45 and 80°. This discrepancy is explained in our previous work, where it is mentioned that low signal to noise at $\theta_i = 45°$ and contamination from non-scattered species entering the detector directly from our molecular beam at $\theta_i = 80°$ provide the most likely explanation for this difference.[29]

Fractional energy losses for the scattering of Ne, CD_4, D_2O, and ND_3 from dodecane as well as Ne, CH_4, D_2O, and NH_3 scattered from squalane at $\chi = 90°$ by Nathanson are shown in Table 2.[32] The average translational energies of each species range from 23.7 to 33.4 kJ mol^{-1} and are all measured at a deflection angle of 90°. The ordering of the fractional energy loss for each scatterer is Ne < CD_4 < ND_3 < D_2O on both squalane and dodecane.

The frequency of the umbrella inversion vibrational mode of ND_3 is significantly lower than the vibrational modes of the other scattered molecules previously scattered on dodecane. However, the presence of this low-frequency mode does not appear to enhance the fractional

11

translational energy loss of ND_3 relative to the other species, so it is reasonable to assume that the internal energy of the scattered ND_3 is primarily taken up by rotation.

Table 2. TD fractions and fractional energy losses for scattered molecules on a dodecane flat liquid jet and a squalane wetted wheel. E_i = 23.7, 29.3, 33.4, and 28.8 kJ mol^{-1} and V = 0.9, 1.9, 3.6, and 2.8 kJ mol^{-1} for Ne, CD_4, D_2O, and ND_3, respectively. All values are taken at χ = 90°. Values for Ne, CD_4, and D_2O scattering from dodecane are reported from our previous work and averaged for all three incident angles.[29] Values for squalane scattering are taken from work performed by Nathanson[32] and interpolated to yield values at the appropriate beam energy for each species.

Scattered Species	Fractional Energy Loss		TD Fraction	
	Dodecane	Squalane[a]	Dodecane	Squalane[a]
Ne (Fast)	0.46	0.42	0.29	0.32
CD_4	0.61	0.49	0.40	0.49
D_2O	0.64	0.56	0.48	0.57
ND_3	0.62	0.52	0.49	0.59

[a]Values for CD_4 and ND_3 are reported for CH_4 and NH_3.

TD Fractions

The TD fraction is defined as the fraction of overall scattering events attributed to thermal desorption. TD fractions are shown in Table 2 and follow a similar trend to the data obtained by Nathanson for squalane, where the TD fraction of Ne is significantly smaller than that of the other scattered species.[32] The overall trend of TD fractions is Ne < CD_4 < D_2O < ND_3 on both dodecane and squalane. Ne has a significantly smaller TD fraction than the molecular scatterers, while CD_4, D_2O, and ND_3 all have similar TD fractions. The increasing trend of the molecular scatterer TD fraction follows and has been attributed to the solubility of these molecules and the free energy of solvation $\Delta G^{\circ}_{solv} = -RT\ln K_H$ in previous work.[29, 32] As seen before, the solubility of the scattered species in dodecane correlates with the TD fraction. Comparing the TD fraction of species scattered on dodecane to Nathanson's work on squalane shows that for all species besides Ne there

12

is a ∼20 % increase in TD fraction on squalane compared to dodecane; this trend is attributed to

squalane being a softer surface than dodecane as mentioned in our previous work.[29]

Conclusions

The evaporation and scattering of ND_3 from a dodecane flat liquid jet have been

investigated and compared to previous work for Ne, CD_4, and D_2O scattered from a dodecane flat

liquid jet, as well as analogous species scattered from squalane on a wetted wheel. Evaporation

experiments were performed to quantify the role that vapor phase interference would pose while

scattering ND_3 from a dodecane flat jet. TOF measurements of ND_3 evaporation were fit to a sum

of two MB distributions comprising a fast contribution from evaporation and a slow contribution

from an isotropic background signal. Good agreement between the fitted data and expected

distributions from an evaporation process suggests that vapor phase interference does not

contribute significantly to the measured evaporation signal.

Scattering experiments were conducted and followed similar trends seen in both our

previous experiments and work by Nathanson on squalane. The angular plots for ND_3 scattering

show that the TD channel for all incident angles obey the $\cos\theta_f$ law well, and the IS channel peaks

at an angle equivalent to or slightly greater than the specular scattering angle for all three incident

angles as expected from previous liquid surface scattering experiments. The TD fractions of the

scattered species show that Ne has similar TD fractions on both dodecane and squalane, while

CD_4, D_2O, and ND_3 have significantly higher TD fractions compared to Ne. The TD fractions of

CD_4, D_2O, and ND_3 on squalane are ∼20 % higher than the analogous scattered species on

dodecane, indicating that squalane is a softer surface than dodecane and therefore is more likely to trap scattered species.

The fractional energy losses for ND_3 were fitted by a soft-sphere model for all three incident angles. When comparing the fractional energy losses of all scattered species, the fractional energy loss on dodecane and squalane follow the trend of $Ne < CD_4 < ND_3 < D_2O$. The fractional energy loss of 0.62 for ND_3 on dodecane follows the trend of the other polyatomic species and is $\sim$10 % greater than the analogous species scattered from squalane.

This work concludes our investigation of small molecule scattering from a dodecane flat jet, and in conjunction with our previous work serves as a proof of concept of elucidating small molecule scattering dynamics from a volatile flat liquid jet. Future directions of this work aim to investigate both non-reactive and reactive scattering from more volatile systems such as water.

Acknowledgments

Author Declarations

Conflicts of Interest

The authors have no conflicts of interest to disclose.

Author Declarations

†S.S. and W.Y. contributed equally.

Steven Saric: Conceptualization (equal); Data Curation (equal); Investigation (equal); Formal Analysis (lead); Methodology (equal); Writing (lead)

Walt Yang: Conceptualization (equal); Data Curation (lead); Investigation (lead); Formal Analysis (equal); Methodology (equal); Writing – review & editing (equal)

Daniel M. Neumark: Conceptualization (lead); Methodology (equal); Project administration (lead); Resources (lead); Supervision (lead); Validation (lead); Writing – review & editing (equal).

Data Availability

The data that support the findings of this study are available from the corresponding author upon reasonable request.

References

1.   A. Singh and M. Agrawal, *J. Environ. Biol.*, 2007, **29**, 15.
2.   R. Putikam and M. C. Lin, *Int. J. Quantum Chem.*, 2018, **118**, e25560.
3.   M. F. Ruiz-Lopez, M. T. Martins-Costa, J. M. Anglada and J. S. Francisco, *J. Am. Chem. Soc.*, 2019, **141**, 16564.
4.   P. M. Haugan and F. Joos, *Geophys. Res. Lett.*, 2004, **31**.
5.   G. Richmond, *Chem. Rev.*, 2002, **102**, 2693.
6.   B. Winter and M. Faubel, *Chem. Rev.*, 2006, **106**, 1176.
7.   G. Rovelli, M. I. Jacobs, M. D. Willis, R. J. Rapf, A. M. Prophet and K. R. Wilson, *Chem. Sci.*, 2020, **11**, 13026.
8.   G. M. Nathanson, *Annu. Rev. Phys. Chem.*, 2004, **55**, 231.
9.   M. E. Saecker, S. T. Govoni, D. V. Kowalski, M. E. King and G. M. Nathanson, *Science*, 1991, **252**, 1421.
10.   J. A. Faust and G. M. Nathanson, *Chem. Soc. Rev.*, 2016, **45**, 3609.
11.   D. R. Herschbach, *Faraday Disc.*, 1973, **55**, 233.
12.   D. M. Neumark, A. M. Wodtke, G. N. Robinson, C. C. Hayden and Y. T. Lee, *J. Chem. Phys.*, 1985, **82**, 3045.
13.   R. E. Continetti, B. A. Balko and Y. T. Lee, *J. Chem. Phys.*, 1990, **93**, 5719.
14.   W. H. Weinberg, *Adv. Colloid Interface Sci.*, 1975, **4**, 301.
15.   J. E. Hurst, C. A. Becker, J. P. Cowin, K. C. Janda, L. Wharton and D. J. Auerbach, *Phys. Rev. Lett.*, 1979, **43**, 1175.
16.   J. A. Barker and D. J. Auerbach, *Surf. Sci.*, 1985, **4**, 277.
17.   U. Harten, A. M. Lahee, J. P. Toennies and C. Wöll, *Phys. Rev. Lett.*, 1985, **54**, 2619.

18. M. J. Cardillo, *Surf. Sci.*, 1994, **299**, 277.
19. Y. Huang, C. T. Rettner, D. J. Auerbach and A. M. Wodtke, *Science*, 2000, **290**, 111.
20. M. E. King, G. M. Nathanson, M. Hanning-Lee and T. K. Minton, *Phys. Rev. Lett.*, 1993, **70**, 1026.
21. G. M. Nathanson, P. Davidovits, D. R. Worsnop and C. E. Kolb, *J. Phys. Chem.*, 1996, **100**, 13007.
22. B. Wu, J. Zhang, T. K. Minton, K. G. McKendrick, J. M. Slattery, S. Yockel and G. C. Schatz, *J. Phys. Chem.*, 2010, **114**, 4015.
23. S. M. Brastad and G. M. Nathanson, *Phys. Chem. Chem. Phys.*, 2011, **13**, 8284.
24. P. D. Lane, K. E. Moncrieff, S. J. Greaves, K. G. McKendrick and M. L. Costen, *J. Phys. Chem. C*, 2020, **124**, 16439.
25. M. Faubel, S. Schlemmer and J. P. Toennies, *At. Mol. Clusters*, 1988, **10**, 269.
26. M. Faubel and T. Kisters, *Nature*, 1989, **339**, 527.
27. J. D. Koralek, J. B. Kim, P. Brůža, C. B. Curry, Z. Chen, H. A. Bechtel, A. A. Cordones, P. Sperling, S. Toleikis and J. F. Kern, *Nat. Commun.*, 2018, **9**, 1353.
28. C. Lee, M. N. Pohl, I. A. Ramphal, W. Yang, B. Winter, B. Abel and D. M. Neumark, *J. Phys. Chem. A*, 2022, **126**, 3373.
29. W. Yang, C. Lee, S. Saric, M. N. Pohl and D. M. Neumark, *J. Chem. Phys.*, 2023, **159**, 1.
30. K. C. Janda, J. E. Hurst, J. Cowin, L. Warton and D. J. Auerbach, *Surf. Sci.*, 1982, **130**, 395.
31. I. Kinefuchi, Y. Kotsubo, K. Osuka, Y. Yoshimoto, N. Miyoshi, S. Takagi and Y. Matsumoto, *Microfluid Nanofluid*, 2017, **21**, 1.
32. M. E. Saecker and G. M. Nathanson, *J. Chem. Phys.*, 1993, **99**, 7056.
33. P. J. Hesse, R. Battino, P. Scharlin and E. Wilhelm, *J. Chem Eng. Data.*, 1996, **41**, 195.
34. P. Schatzberg, *J. Phys. Chem.*, 1962, **67**, 776.
35. D. C. Ghosh, J. Jana and R. Biswas, *Int. J. Quantum Chem.*, 2000, **80**, 1.
36. J. R. Letelier and C. A. Uteras-Diaz, *Spectrochim. Acta A Mol. Biomol. Spectrosc.*, 1997, **53**, 247.
37. N. O. J. Malcolm and P. L. A. Popelier, *J. Phys. Chem. A*, 2001, **105**, 7638.
38. T. Shimanouchi, *Tables of Molecular Vibrational Frequencies*, 1976.
39. K. Ishida, *BCSJ*, 1958, **31**, 143.
40. Y. T. Lee, J. D. McDonald, P. R. LeBreton and D. R. Herschbach, *Rev. Sci. Instrum.*, 1969, **40**, 1402.
41. Y. T. Lee, *Angew. Chem., Int. Ed. Engl.*, 1987, **26**, 939.
42. D. Irimia, D. Dobrikov, R. Kortekaas, H. Voet, D. A. van den Ende, W. A. Groen and M. H. Janssen, *Rev. Sci. Instrum.*, 2009, **80**, 3303.
43. C. Meng and M. H. Janssen, *Rev. Sci. Instrum.*, 2015, **86**, 13251.
44. E. H. Kennard, *Kinetic theory of gases*, McGraw-hill New York, 1938.
45. Z. R. Kann and J. L. Skinner, *J. Chem. Phys.*, 2016, **144**, 154701.
46. F. B. Dunning and R. G. Hulet, *Atomic, molecular, and optical physics: Atoms and molecules*, Academic press, 1996.
47. A. Lebéhot, J. Kurzyna, V. Lago and M. Dudeck, in *Atomic and Molecular Beams: The State of the Art 2000*, ed. R. Campargue, 2001, pp. 237.
48. M. E. King, K. M. Fiehrer and G. M. Nathanson, *J. Phys. Chem.*, 1997, **101**, 6556.
49. B. G. Perkins and D. J. Nesbitt, *J. Phys. Chem.*, 2009, **113**, 4613.
50. R. B. Subbarao and D. R. Miller, *J. Chem. Phys.*, 1973, **58**, 5247.

51.   C. T. Rettner, L. A. DeLouise and D. J. Auerbach, *J. Chem. Phys.*, 1986, **85**, 1131.
52.   C. T. Rettner and M. N. R. Ashfold, *Dynamics of gas-surface interactions*, 1991.
53.   W. A. Alexander, J. Zhang, V. J. Murray, G. M. Nathanson and T. K. Minton, *Faraday discussions*, 2012, **157**, 355.
54.   N. Andric and P. Jenny, *Phys. Fluids*, 2018, **30**, 7104.
55.   F. M. Mourits and F. H. A. Rummens, *Can. J. Chem.*, 1977, **55**, 3021.
56.   H. A. Lorentz, *Ann. Phys.*, 1881, **248**, 127.

Figure Captions

Figure 1. Instrument schematic for scattering experiments performed in this work. Dashed lines indicate the molecular beam (red trace) striking the liquid surface and scattering from it (blue trace). Inset in the bottom right shows the incident angle θ_i, the scattering angle θ_f, and the deflection angle $\chi = 180° - (\theta_i + \theta_f)$.

Figure 2. Normalized evaporation TOF spectra of ND_3 from a ND_3-doped liquid dodecane flat jet at 269 K. TOF distributions are fitted with a linear combination of Maxwell–Boltzmann velocity distributions at the liquid temperature (blue traces) and at $T_{bkg} = 75$ K (light blue traces). The absolute intensity of the T_{bkg} component is fixed for all angles. The green traces represent the sum of the two contributions.

Figure 3. Angular plot created from the integrated, non-normalized intensities of the Maxwell–Boltzmann simulations at T_{liq} and T_{bkg} (blue circles and cyan triangles, respectively) of ND_3 evaporation data at various detector angles. The cosine function representing the expected angular distribution for evaporation is indicated by the dashed gray curve.

Figure 4. Normalized TOF spectra of ND_3 scattering ($E_i = 28.8$ kJ mol^{-1}) from a dodecane flat liquid jet with (a) $\theta_i = 45°$, (b) $\theta_i = 60°$, and (c) $\theta_i = 80°$. The data are fitted by the sum of an SS distribution (red traces) and an MB distribution (blue traces) at the liquid jet temperature ($T_{liq} = 269$ K). The sum of the two contributions is shown by the green traces.

Figure 5. Angular plots created from the integrated, non-normalized intensities of scattering at incident angles of (a) 45°, (b) 60°, and (c) 80°. Blue squares represent the TD, and red circles represent the IS contributions to the TOF fits. The cosine function representing the expected angular distribution for evaporation is indicated by the dashed gray curves. Arrows indicate the specular angle.

Figure 6. Average fractional energy loss as a function of deflection angle for impulsively scattered ND_3 from a dodecane flat jet at 269 K. The incident translational energy is 28.8 kJ mol^{-1} and the gas-surface potential is modeled as 2.8 kJ mol^{-1}. The fractional energy loss at incident angles of 45, 60, and 80° are displayed as black squares, red circles, and blue triangles respectively. The solid curve gives a prediction for the soft-sphere model, while the dashed curve gives a prediction for the hard-sphere model where internal excitation has been set to zero. The fitted parameters are $m_{eff} = 55$ amu and $E_{int} = 5.08$ kJ mol^{-1} for the soft-sphere model, and $m_{eff} = 36$ amu and $E_{int} = 0$ kJ mol^{-1} for the hard-sphere model.
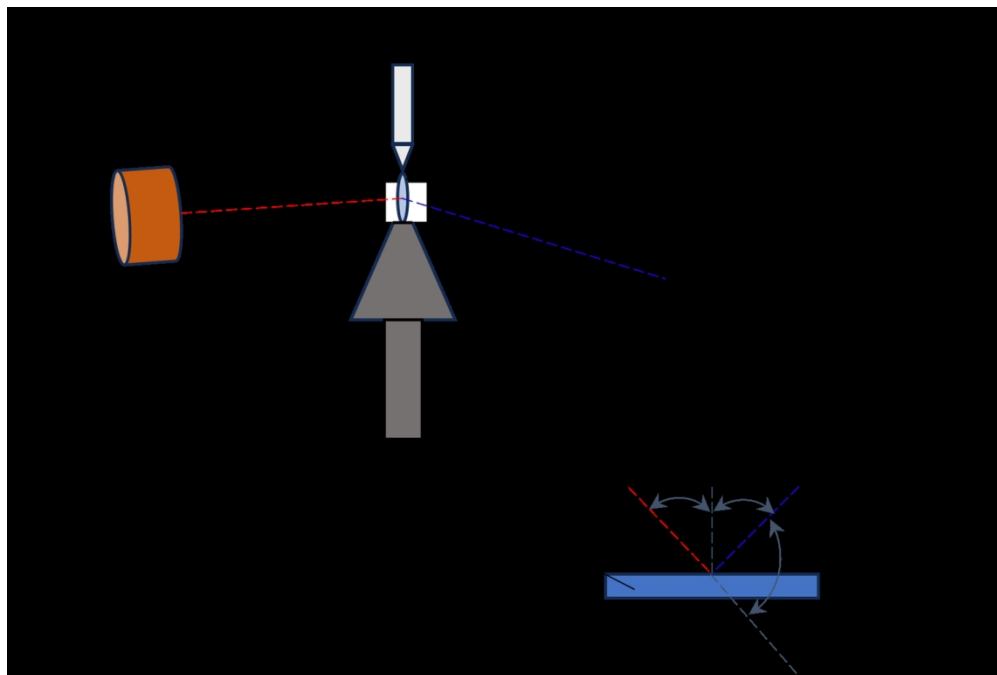
128x86mm (300 x 300 DPI)
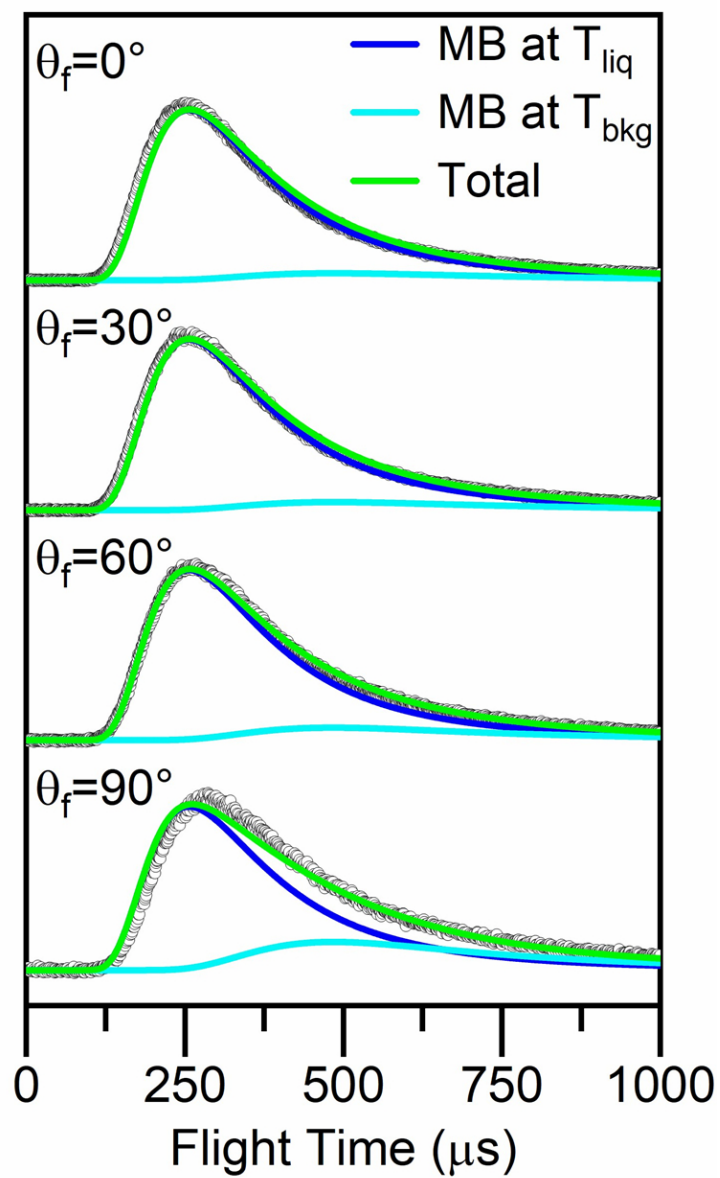
63x106mm (300 x 300 DPI)
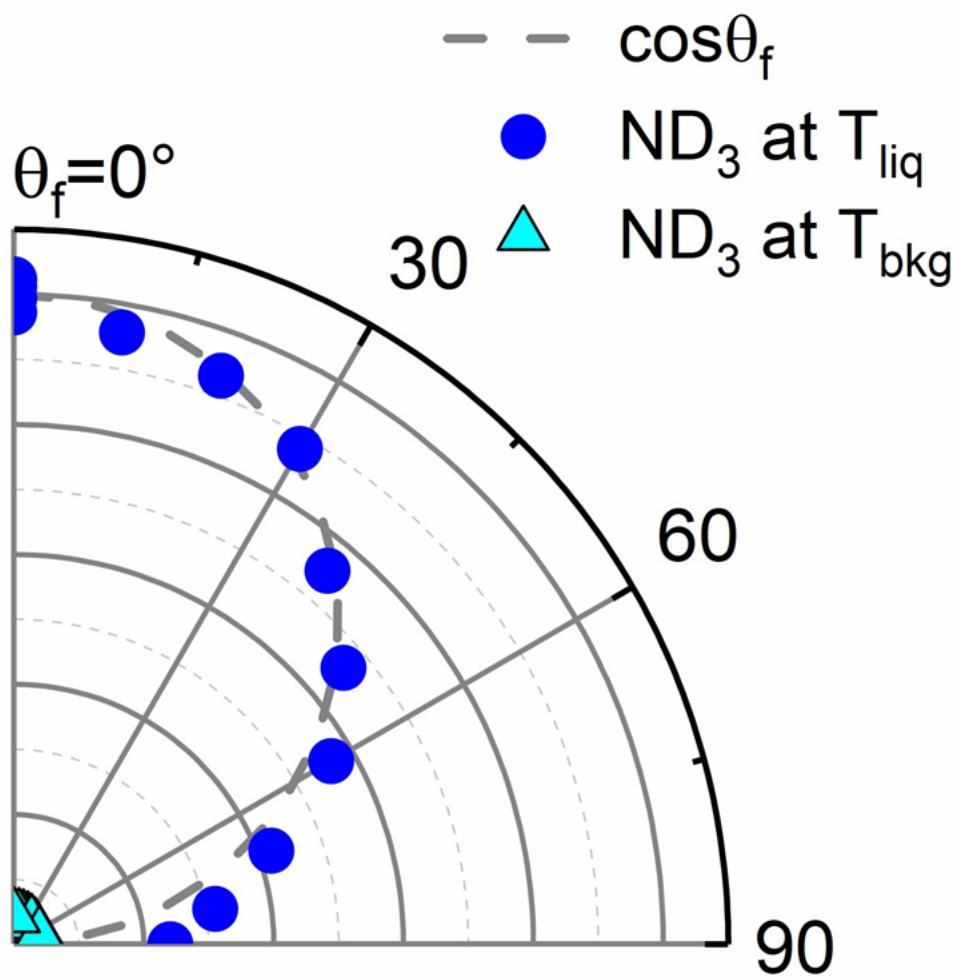
63x63mm (300 x 300 DPI)
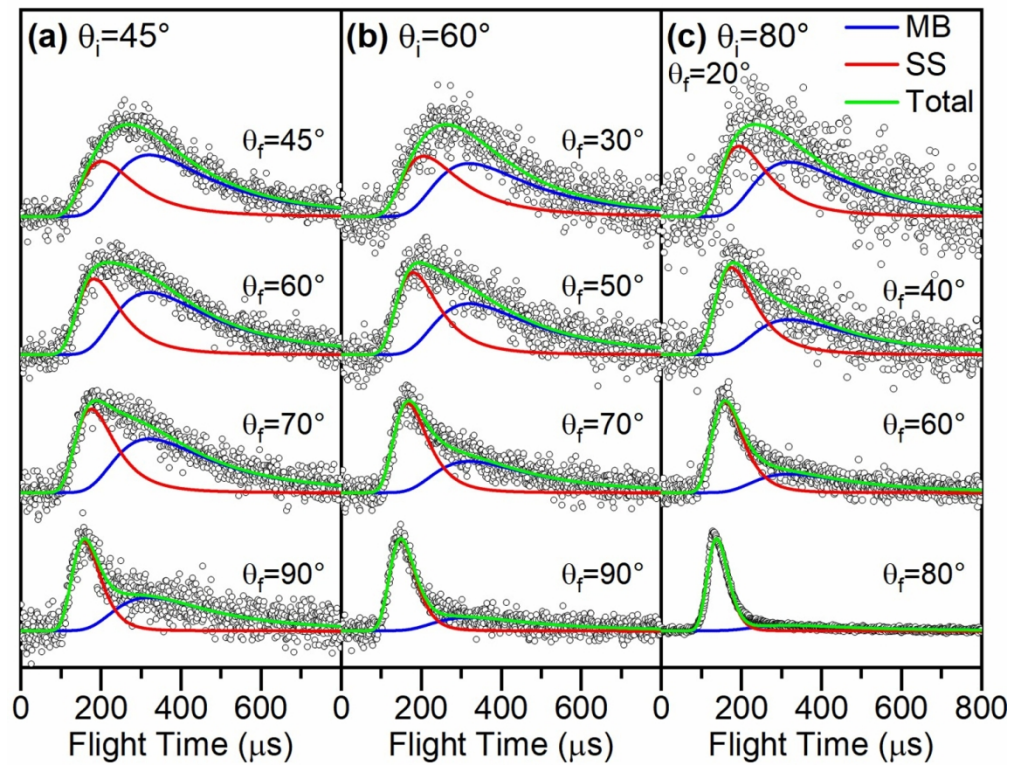
127x97mm (300 x 300 DPI)
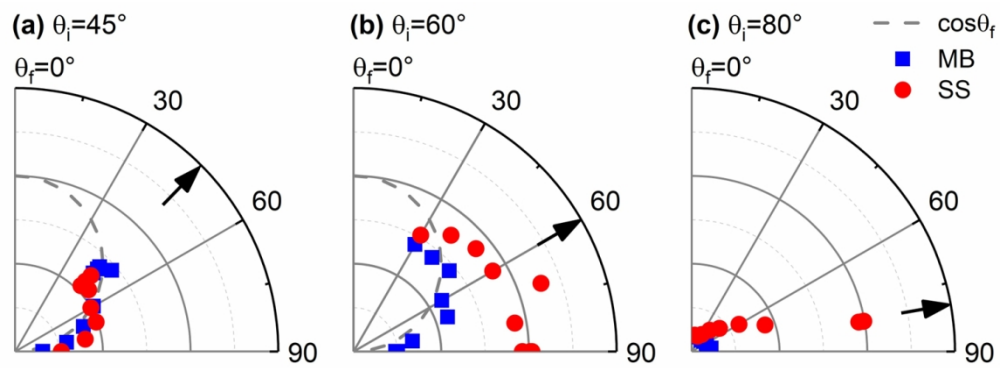
127x46mm (300 x 300 DPI)

101x76mm (300 x 300 DPI)